Int. J. Electrochem. Sci., 12 **(2017)** 8929 – 8943, doi: 10.20964/2017.10.46

International Journal of
ELECTROCHEMICAL
SCIENCE
www.electrochemsci.org

Study of the pitting corrosion at welding joints of Inconel 625 alloy under high temperature and high H_2S/CO_2 partial pressure

Qiang Guo[1,2], *Yuan Li*[1,2], *Jiong Qian*[1,2], *Haobo Yu*[1,2], *Changfeng Chen*[1,2,*]

[1] College of Mechanical and Electrical Engineering, China University of Petroleum (Beijing), No.18 FuXue road, ChangPing district, Beijing, 102249, China
[2] Beijing Key Laboratory of Failure, Corrosion and Protection of Oil/gas Facilities, China University of Petroleum (Beijing), Changping District, Fuxue Road 18, Beijing 102249, P. R. China.
[*]E-mail: tyhb_yu@163.com

Received: 19 March 2017 / *Accepted:* 6 August 2017 / *Published:* 12 September 2017

The corrosion resistances of the Incoloy 825 alloy base metal and the Inconel 625 alloy weld under high temperature high pressure (HTHP) H_2S/CO_2 conditions were investigated. Pitting was only presented on the Inconel 625 alloy weld, even though it contains more corrosion-resistant elements than the Incoloy 825 alloy. Laves and G phases were found in the 625 alloy weld, which were confirmed to possess a lower corrosion resistance than the matrix using scanning Kelvin probe force microscopy. The changes in the semiconductor structure of the passive films were analysed through the Mott–Schottky curves after the HTHP H_2S/CO_2 corrosion. Finally, the pitting mechanism of Inconel 625 weld was discussed.

Keywords: G phase, Laves phase, Mott–Schottky plot, Pitting corrosion, H_2S/CO_2 corrosion

1. INTRODUCTION

Increasing energy costs and the growing demand for natural gas have driven the development of sour gas exploitation around the world [1]. However, sour gas is highly corrosive due to the presence of H_2S, CO_2, Cl^-, and free sulphur, as well as a high operating temperature (up to 200 °C). Therefore, the exploitation of high H_2S content sour gas fields is very dangerous because the leakage of sour gas caused by high temperature and high pressure (HTHP) H_2S corrosion will not only lead to explosion but also cause significant casualties and economic loss due to the extremely toxicity of H_2S. Incoloy 825 (UNS N08825) is a solid solution strengthening nickel-iron-chromium alloy with additions of molybdenum, copper, and titanium that provides exceptional resistance to corrosive environments. Therefore, it is considered an appropriate material for sour gas/oil exploitation

equipment, such as well tubes and ground gathering pipelines [2]. Moreover, the austenitic solid solution strengthening nickel-chromium-molybdenum alloy Inconel 625 (UNS N06625) has favourable welding and mechanical properties. Therefore, it is usually chosen as the welding material for Incoloy 825. Meanwhile, the higher alloy content in Inconel 625 makes it more resistant to a severe corrosive environment than Incoloy 825 [3].

It is well known that niobium and molybdenum are important solid solution strengthening elements in Inconel 625. They can be precipitated as the forms of γ'' or δ intermetallic phase (Ni_3Nb) and carbides during the high temperature ageing treatment, which then strengthens the matrix [4]. However, the distribution coefficients of Nb and Mo are lower than 1. Accordingly, they will segregate to the liquid metal, enriching in the interdendritic region and depleting in the dendrite core at the final stage of solidification [5, 6]. Therefore, the welding process of Inconel 625 is often associated with severe segregation of Nb and Mo and the formation of intermetallic compounds in the interdendritic region, which is denoted as the Laves phase and represented as $(Ni, Cr, Fe)_2(Nb, Mo, Ti)$ [7, 8].

The corrosion performance of Inconel 625 weld is directly affected by the alloy microstructure [8]. In a relatively mild corrosive environment, such as seawater, the corrosion resistance of Inconel 625 weld is equivalent to that of base metal [9]. However, in aggressive environments, the segregation behaviour in Inconel 625 welds is reported to be detrimental to its pitting and crevice corrosion resistance [8-14]. The corrosion mainly occurs in the interdendritic region, where the protection of passive film is reduced by the depletion of Ni and Cr [11, 12, 15]. Ahmed and Cooper suggested that the localized corrosion mechanism of Inconel 625 weld was related to the galvanic corrosion between the interdendritic region (or Laves phase) and the dendrite core [9, 11]. Zahrani considered that Laves phase was a suitable site for the initiation and growth of pits, which ultimately led to the development of the internal attacked area [8].

High temperature and high pressure (HTHP) H_2S sour gas is a very aggressive environment, in which the passive film of nickel alloys will change from a compact oxide passive film into the less protective sulphide film [16], resulting in localized corrosion. At the same time, welding is a complex thermal cycle process, so it is difficult to eliminate the Nb and Mo segregation and the Laves formation in Inconel 625. Therefore, it is important to clarify how the element segregation, Laves phase, and base metal (for example, Incoloy 825) influence the corrosion resistance of the Inconel 625 weld under a HTHP H_2S sour gas environment. However, no relevant research has been reported to date.

In this study, the corrosion characteristics of the Inconel 625 weld and the Incoloy 825 base metal in a high H_2S content environment were studied. The mechanism of the pitting corrosion formed on the Inconel 625 weld is discussed based on the analysis to the elemental segregation, the precipitation of second phase, the Kelvin potential distribution in the Inconel 625 weld bead, and the semiconductor structure conversion of the passive film during the HTHP H_2S/CO_2 corrosion. The objective of the present paper is to provide support for the safe control of the Inconel 625 weld in the service in a high sour gas field.

2. EXPERIMENTAL MATERIAL AND METHODS

The base metal is the as-received solution annealed Incoloy 825 pipe (ϕ114×16), and a standard V-Butt configuration (single V-groove with a root gap of 2 mm, a size land of 1 mm and an included angle of 70°) was used for gas metal arc welding (GMAW). The Inconel 625 welding wire with a diameter of 1.2 mm was used, which was supplied by the VBC group, Lough-borough, UK. The chemical compositions of these two alloys are presented in Table 1.

Table 1. The chemical compositions of the filler and base metals in wt%.

Element	C	Ni	Cr	Mo	Fe	Si	Mn	Ti	Cu	Al	P	S
Inconel 625	0.028	Bal	22.18	8.86	4.32	0.28	0.08	0.26	-	0.28	0.03	0.002
Incoloy 825	0.04	40.21	20.45	3.10	Bal	0.30	0.07	0.88	2.42	0.11	0.03	0.03

The welding parameters were set as the following: 120-140 A welding current; 20–24 V welding voltage; 17–25 cm/min welding speed; 10–16 kJ/cm welding energy; 6–9 m/min wire feed rate; 15 L/min shielding gas flow; and a 10 mm distance from the tip of the electrode to the work piece. After welding, the samples were cut from the weld metal and prepared for metallographic analysis and corrosion tests.

Microstructures were examined with a scanning electron microscope (SEM) (FEI Quanta 200F) equipped with an energy dispersive X-ray spectroscopy (EDS) system. Samples were also characterized by transmission electron microscopy (TEM) using an FEI Tecnai G2 F20 microscope coupled with an EDS microanalysis system.

SKPFM measurements were performed with a MultiMode TM Nanoscope IX atomic force microscope (AFM) from Veeco Instruments Inc. The tips used were the Nanoprobe TM SCM-PIT conductive PtIr-coated silicon tip with a force constant of 2.5 N/m and a resonant frequency of 60-100 kHz. The SKPFM analysis was performed on polished samples in air at room temperature.

Table 2. Experimental conditions.

Condition no.	Temperature (℃)	H_2S (MPa)	CO_2 (MPa)	Medium	Period (h)
1	150	3.5	3	15% NaCl solution	720
2	205				

HTHP H_2S/CO_2 corrosion tests were carried out in an autoclave (C-276 autoclave system, Cortest Inc), using the test conditions shown in Table 2. The weight loss test samples with the weld bead at the centre, sized at 67.5 × 4.75 × 1.5 mm, were abraded and polished with a 0.5 μm grade

paste. Before the test, the autoclave was deaerated using high purity N_2 for at least 2 h, and then, the required partial pressure of H_2S/CO_2 and temperature were set in the system. The experiment started after reaching the specified testing conditions. After 720 h, the corrosion specimens were taken out from the autoclave, sequentially rinsed with distilled water and absolute alcohol, and then dried in air. After the tests, the specimen surface was observed with SEM.

Electrochemical measurements were performed using a CHI660C electrochemical workstation. A classical three electrode cell was used for the electrochemical tests with a platinum plate as the counter electrode and a saturated calomel electrode (SCE) as the reference electrode.

The working electrodes, ϕ10×5 mm in dimension, were cut from the Incoloy 825 base metal and the Inconel 625 weld. All the electrodes were sealed with epoxy, and a conductive wire was soldered to the back for the electrochemical measurements. The surfaces were mechanical abraded and polished with 0.5 μm grade paste. Then, the electrodes were corroded in the autoclave under HTHP H_2S/CO_2 conditions. Electrochemical tests were carried out with these corroded electrodes and compared with the uncorroded samples. All the electrochemical tests were performed at ambient temperature (25 ℃) with continuous N_2 bubbling. The electrolyte for the tests was a 5 wt% Na_2SO_4 solution with its pH adjusted to 4.0 by using H_2SO_4. The solutions were prepared from analytical grade reagents and twice-distilled water.

The potentiodynamic polarization curve was measured at a potential sweep rate of 1 mV/s. The Mott–Schottky plot measurements were carried out at 1000 Hz in the potential range from -1 to 0.8 V, with a perturbing signal of 50 mV.

3. EXPERIMENTAL RESULTS AND DISCUSSION

3.1 Macrostructure of the weld bead

The microstructures of the Incoloy 825 base metal, weld fusion line region and Inconel 625 weld bead are presented in Fig. 1.

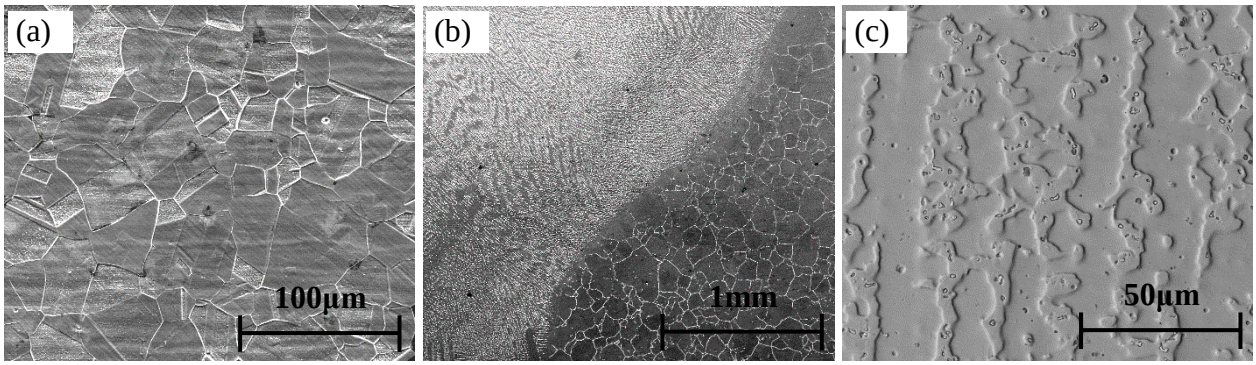

Figure 1. SEM microstructure of the Incoloy 825 base metal (a), weld fusion line region (b) and Inconel 625 weld bead (c).

The grains of the solution annealed Incoloy 825 base metal are equiaxial (Fig. 1(a)). There is no significant change could be observed in the grain size in the heat affected zone, and no precipitates are found within the grain boundaries. The Inconel 625 filler metal shows solidification microstructures and exhibits a proper fusion with the base metal (Fig. 1(b)). However, in the weld bead, granular and strip-like precipitates are observed in the interdendritic regions (Fig. 1(c)).

The present precipitates were observed by transmission electron microscopy (TEM), as shown in Fig. 2. Two main types of secondary phases were confirmed by analysing to the selected area electron diffraction (SAED) pattern. One observed phase is the Laves phase, which is in the $MgZn_2$ type (point group is C14) structure. Its lattice constants are a = 0.518 nm and c = 0.852 nm (Fig. 2(a)). The other observed phase is the G phase, which has an FCC lattice structure (constant a = 1.14 nm), similar to the $M_{23}C_6$ (lattice constant a = 1.065 nm) and M_6C (lattice constant a = 1.12 nm) precipitates (Fig. 2(b)) [17-19].

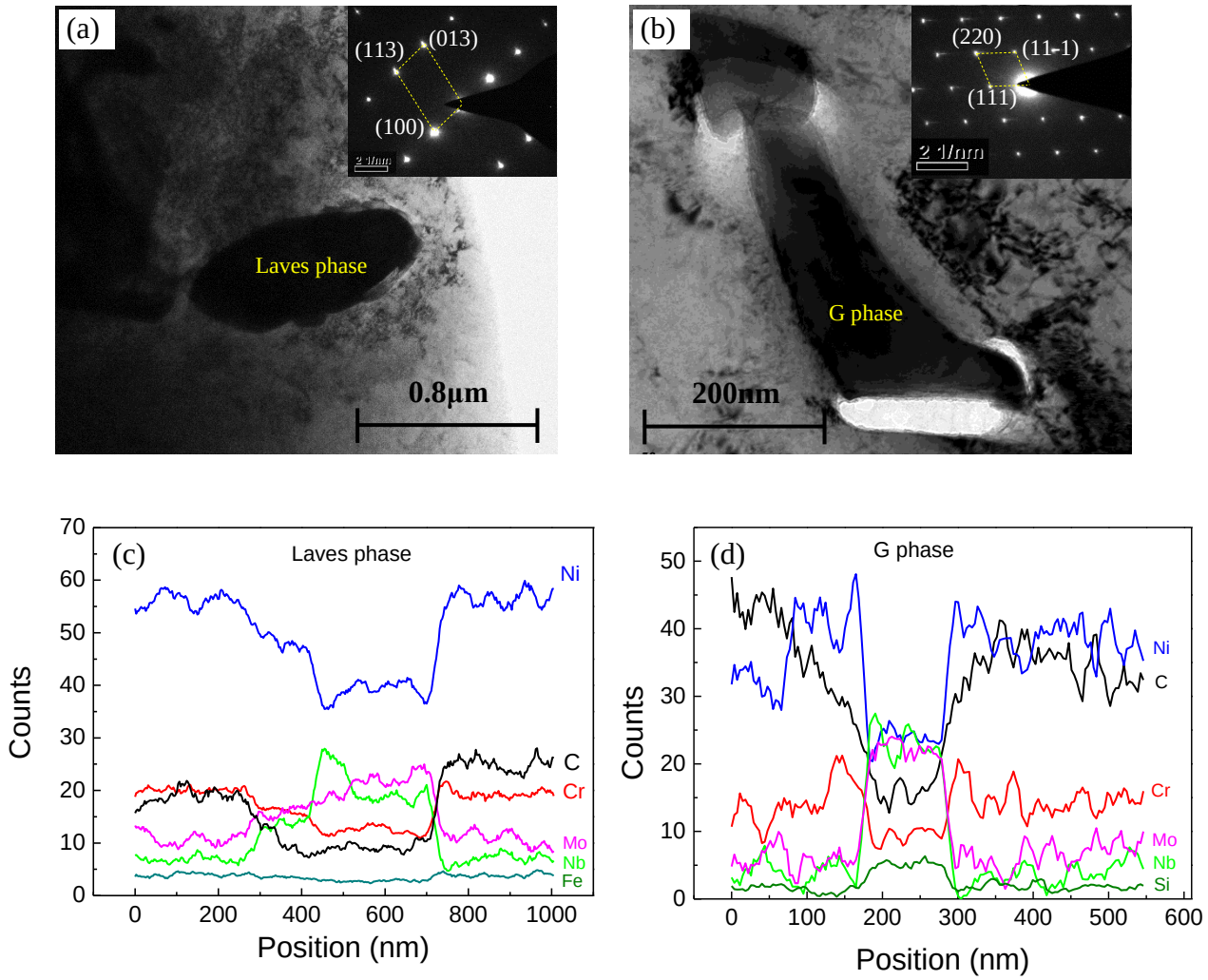

Figure 2. TEM micrographs and SAED patterns of the Laves phase (a) and G phase (b), and the TEM/EDS line distribution of the chemical composition of the Laves phase (c) and G phase (d) in the Inconel 625 weld bead.

The Laves phase is a common precipitate that exists in the Inconel 625 alloy solidification microstructure. It is dominated by the segregation behaviour of Nb and the formation of Nb-rich, eutectic-like constituents in the form of γ/laves. Si and C will also influence the minor constituent population [20]. Using TEM/EDS, the chemical composition of the Laves phase is determined, as shown in Fig. 2(c). It is seen that the contents of Ni, Cr and C in the Laves phase are significantly lower than those in the matrix metal, while the contents of Nb and Mo have the opposite behaviour. It is known that Ni and Cr are important alloy elements for corrosion resistance. Therefore, the reduction of Ni and Cr content will degrade the corrosion resistance of the Laves phase.

The G phase is an intermetallic silicide, and its stoichiometry is based on the ideal formula of $Ni_{16}Si_7Ti_6$ with possible substitutions of Ni and Ti by Cr, Fe, Mo, Mn, V, Hf, Ta, Zr and Nb [17-19]. It can be precipitated by spinodal decomposition in stainless steels or transformed from Nb(CN) by alloy elemental diffusion in Fe–Ni-based super alloys after long-term ageing [21-25]. However, at present, there are no reports on the formation of the G phase in the Inconel 625 alloy. According to the TEM/EDS spectrum for the elemental line distribution shown in Fig. 2(d), the Si content in the precipitate is much higher than that in the matrix metal, and the relative C content is extremely low. The high Si and low C levels are indicative of the G phase rather than M_6C or $M_{23}C_6$. In general, the size of the G phase is only at the nanometre level [20-25]. However, in Fig. 2(b), the size of the G phase is approximately 0.5 μm. Considering that the thermal welding process is less than 2 hours, there is no sufficient time for elemental diffusion in the alloy. Therefore, the G phase in the Inconel 625 weld bead may form during the welding solidification process. Similar to the Laves phase, the Ni and Cr content in the G phase are relatively low, indicating that the corrosion resistance of the G phase will be lower than that of the matrix metal.

The locations of the Laves phase and G phase can be determined based on their size and composition, as shown in Fig. 3. The Laves phase is an irregular strip and is distributed in the centre of the interdendritic region. The small granular precipitate is the G phase, which preferentially appears at the edges of the interdendritic region. The EDS also shows that there are also a few Al and Ti oxides in the interdendritic region (Fig. 3(a)).

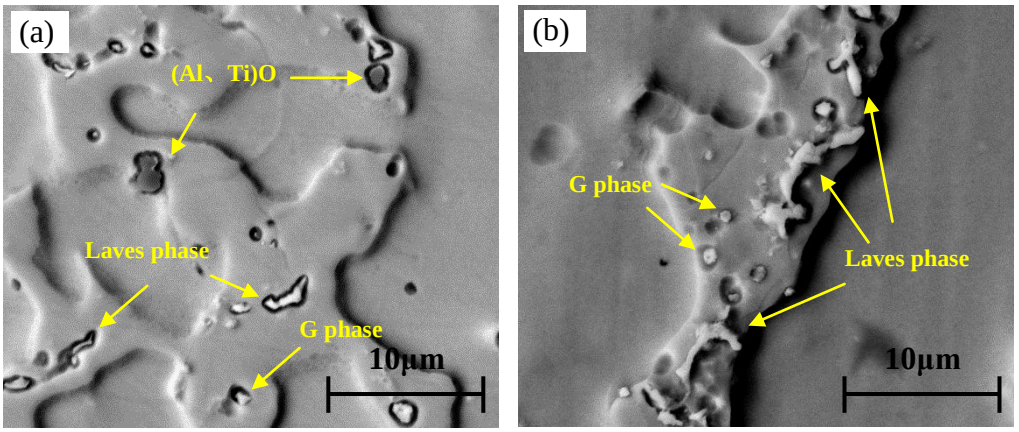

Figure 3. The second phase morphology along a cross section (a) and a lengthwise section (b) of the interdendritic region in the Inconel 625 weld bead.

The compositions of the G phase, Laves phase, interdendritic region and dendrite centre region are listed in Table 3. It can be seen that Nb and Mo are strongly segregated to the G phase and Laves phase. Therefore, the Nb and Mo contents in the G phase and Laves phase are several times higher than those in the interdendritic region. In contrast, Cr and Ni are mainly located in interdendritic region and the dendrite centre and slightly decline in the area relative to the dendrite region. However, the contents of Cr and Ni in the G phase and Laves phase significantly decreases. In particular, the Cr content in the G phase is less than 12 wt%, which will significantly weaken its corrosion resistance.

Table 3. Measured compositions (wt%) of different microstructures in the Inconel 625 weld.

wt%	Cr	Ni	Mo	Nb	Si	Fe
G phase	11.66	30.52	23.62	30.72	3.49	-
Laves phase	19.84	32.64	29.86	13.98	1.27	0.88
interdendritic region	21.24	59.23	8.74	6.25	-	4.54
dendrite centre	21.85	65.41	7.56	-	-	5.17

3.2 SKPFM analysis

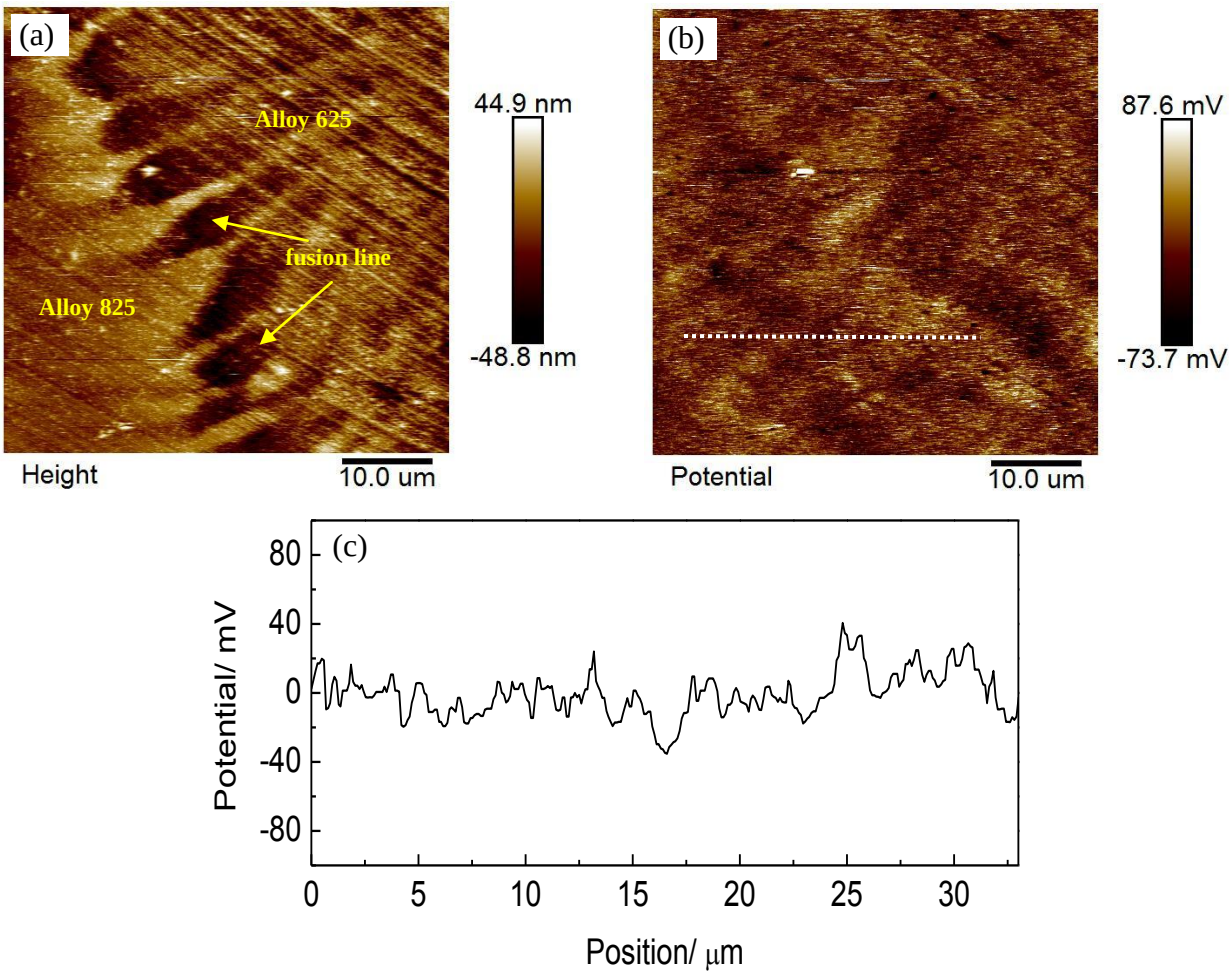

Figure 4. Topography (a) and Volta potential (b) images of the same surface area along the fusion line. The Volta potential profiles (c) performed along the dotted line indicated in (b).

A Kelvin probe is a technique used to measure the surface potential (or Volta potential) of metals in vacuum or air. It is demonstrated that the Volta potential measured with a Kelvin probe has a linear relationship with the corrosion potential under a thin electrolyte layer [26-28]. Scanning Kelvin probe force microscopy (SKPFM) combines the classical Kelvin probe technique with atomic force microscopy, allowing simultaneous mapping of the topography and Volta potential distribution on the passive surface in air. This technique has previously been successfully used for ex situ corrosion studies to test the Volta potential difference between precipitates and the matrix and to analyse the galvanic corrosion tendency [29-34].

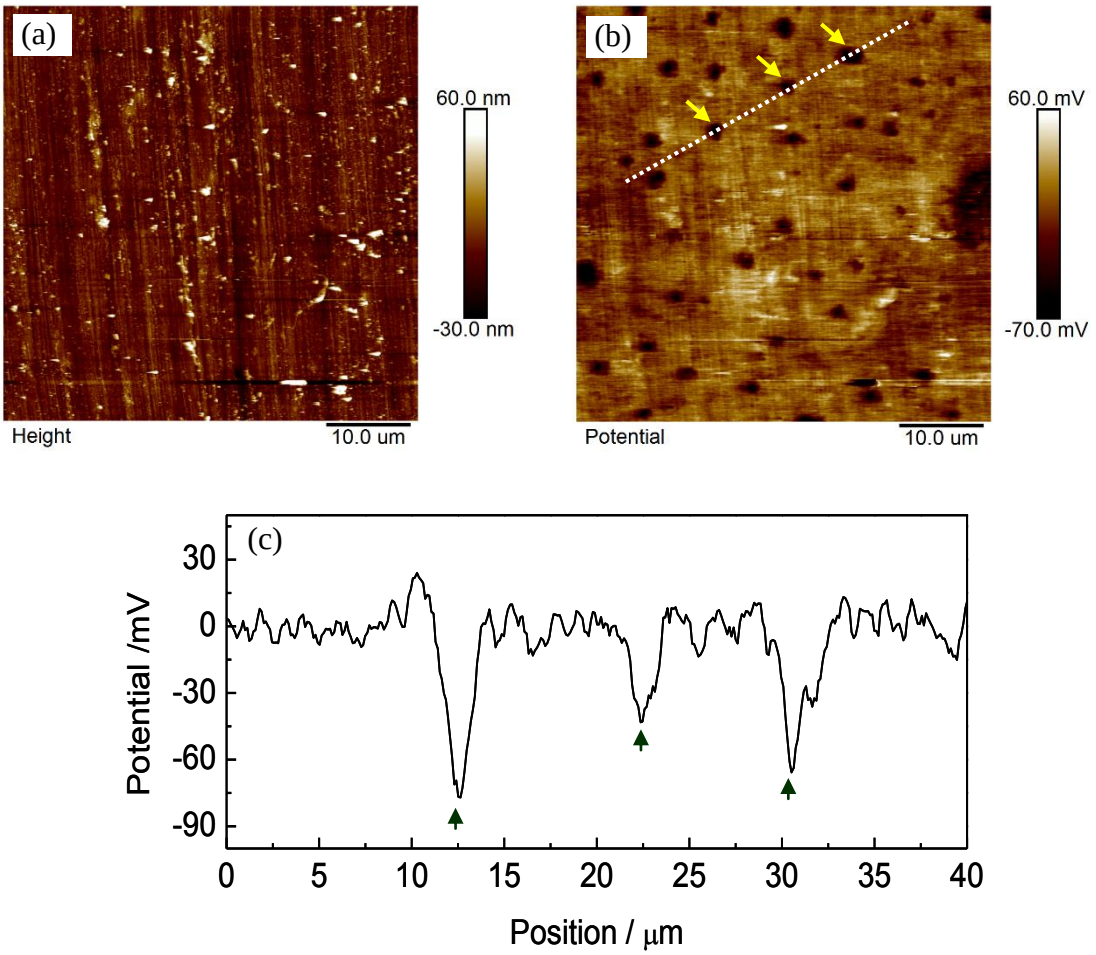

Figure 5. Topography (a) and Volta potential (b) images of the same surface area in the Inconel 625 welding bead. Volta potential profiles (c) performed along the dotted line indicated in (b).

The AFM topography imaged at the fusion line region is shown in Fig. 4(a). There is a clear boundary between the Inconel 625 welding bead and the Incoloy 825 matrix. Fig. 4(b) shows the concurrent SKPFM surface potential mapping at the fusion line region. The lighter areas indicate a higher measured potential [29-34]. There is no obvious potential difference between the Inconel 625 welding bead and the Incoloy 825 matrix. In Fig. 4(c), the fluctuation of the surface potential distribution along the Incoloy 825 matrix, fusion line region, and Inconel 625 welding bead is less than

40 mV (marked in Fig. 4(b)), indicating a similar galvanic corrosion resistance between these two regions.

Fig. 5(a) and Fig. 5(b) are the AFM topographical image and the concurrent SKPFM surface potential mapping of the Inconel 625 welding bead, respectively. Fig. 5(a) displays the scratches on the polished surface. In the surface potential mapping (Fig. 5(b)), several low potential positions with a diameter of approximately 1-2 μm are distributed evenly along the Inconel 625 welding bead. The potentials at these positions are nearly 80 mV lower than those in the surrounding areas, as shown in Fig. 5(c), indicating a relatively low corrosion resistance at these specific points. According to the morphology and composition of the precipitates shown in Fig. 3 and Table 3, these low potential positions are more likely to be the Laves phase or G phase.

3.3 High Temperature High Pressure H_2S/CO_2 Corrosion

After 30 days of H_2S/CO_2 corrosion at 150 ℃, the specimen surface of the Incoloy 825 with an Inconel 625 weld still exhibits its metallic properties, which means that the corrosion conditions cause limited damage to the substrate. In contrast, the surface of the specimen changes to black after being corroded in an H_2S/CO_2 environment at 205 ℃ for 30 days. Scanning electron microscopy observations show that the specimen surface is covered by a fine corrosion scale of (Ni, Cr, Fe)S, as seen in Fig. 6(a). After removal of the corrosion products, several pits in the dendritic structure of the Inconel 625 weld are revealed, with the maximum pit diameter of approximately 50 μm, while the Incoloy 825 base metal presents a uniform corrosion morphology.

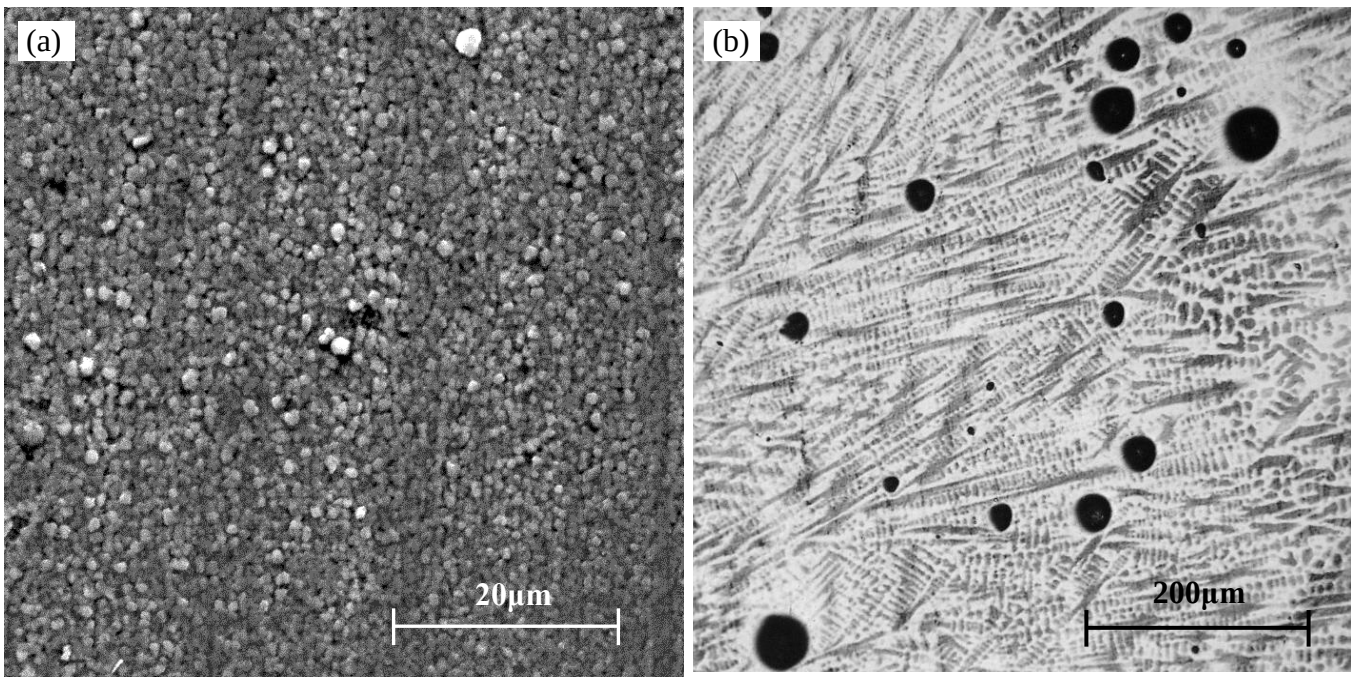

Figure 6. Morphology of the corrosion products on the specimen surface (a) and the pit distribution in the Inconel 625 weld bead (b) after being corroded in a 205℃ H_2S/CO_2 environment for 30 days.

3.4 Electrochemistry measurements

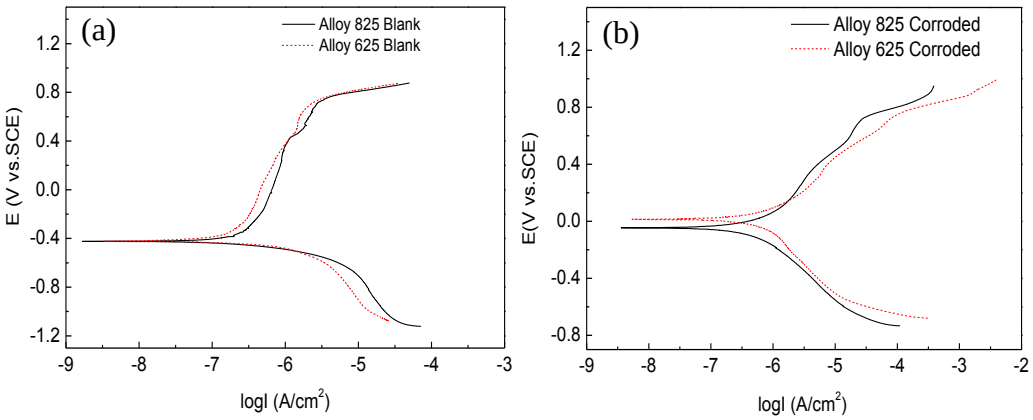

Figure 7. Potentiodynamic polarization curves of the Incoloy 825 base metal and Inconel 625 weld bead for a blank sample (a) and samples corroded in an H_2S/CO_2 environment at 205℃ (b).

Fig. 7 shows the polarization curves of the uncorroded Incoloy 825 base metal and the Inconel 625 weld (Fig. 7(a)) and the same samples after being corroded in an H_2S/CO_2 environment at 205 ℃ (Fig. 7(b)). Electrochemical parameters, such as the corrosion potential (E_{corr}) and the corrosion current density (i_{corr}), obtained from polarization curves using Tafel extrapolation, are presented in Table 4.

Table 4. Electrochemical parameters obtained from the polarization curves of Figure 7.

Samples	Condition	E_{corr} (mV vs. SCE)	i_{corr} (mA/cm^2)	β_a (mV/decade)
Incoloy 825 base metal	without corrosion	-0.423±0.002	2.10±0.03×10^{-4}	668±9
	after corrosion	-0.046±0.001	7.94±0.21×10^{-4}	547±15
Inconel 625 weld bead	without corrosion	-0.421±0.001	1.87±0.15×10^{-4}	944±36
	after corrosion	0.014±0.003	1.11±0.25×10^{-4}	432±6

According to the polarization curves, both of the uncorroded specimens show an obvious passive region and a similar passive potential range. The Inconel 625 weld shows slightly lower i_{corr} compared with the Incoloy 825 base metal, indicating the higher protective performance of the passive film formed on Inconel 625. However, after corrosion in the HTHP H_2S/CO_2 environment, their passive potential ranges become narrow. Furthermore, the polarizability of the passive region becomes diminished, and the values of i_{corr} increase dramatically. This indicates that the density of the passive film is undermined under the corrosive circumstances and that the corrosion rate of the metal matrix is boosted. In addition, the Inconel 625 weld shows a higher i_{corr} value than the Incoloy 825 base metal after being corroded, which means that the Inconel 625 weld is more sensitive than the Incoloy 825 base metal when corroded under an HTHP H_2S/CO_2 environment.

Characterization of the electronic structure of the passive films formed on the specimens in this study was achieved using a Mott–Schottky analysis. It can be found that the plots of C^{-2} vs. E for the passive films formed in air on the Incoloy 825 base metal (Fig. 8(a)) and the Inconel 625 weld (Fig. 8(b)) are qualitatively similar. Therefore, the passive films exhibit the same electronic characteristic. In the depletion region from −0.7 to 0.3 V, there are two linear regions with a positive slope at higher potential and a negative slope at lower potential.

Nickel-based alloys could form a double layer passive film when exposed under air conditions. The outer layer is composed of chrome hydroxide, while the inner layer is comprised of chrome oxide. This type of passive film reflects the characteristics of bipolar semiconductors, with the outer and inner layers acting as p-type and n-type semiconductors, respectively [16, 36], as illustrated in Fig. 8e. When a bipolar passive film is immersed in a solution, two space charge regions can be identified, namely, the space charge region at the interface between the passive film and the solution (C_p) and the space charge generated by the p–n junction (C_{pn}). The band structure of the bipolar passive film is shown in Fig. 8e. The total space charge capacitance of the bipolar passive film C_{total} can be regarded as the series connection of C_{np} and C_p, resulting in two liner regions with reversed slopes in the Mott–Schottky plots of C^{-2} vs. E, as shown in Fig. 8a. Based on the relationship between the space charge capacitance of the bipolar passive film and the applied potential deduced in our previous work [16], the C^{-2}_p, C^{-2}_{pn}, and C^{-2}_{total} vs. E plots can be analysed using the non-linear fitting method (Fig. 8a), and the majority carriers' density is calculated and summarized in Table 5. According to the fitting results, the inner n-type semiconductor layer is highly protective for the metal matrix because of its higher compact density. Furthermore, the passive film formed on the Inconel 625 weld is more protective than that on the Incoloy 825 alloy.

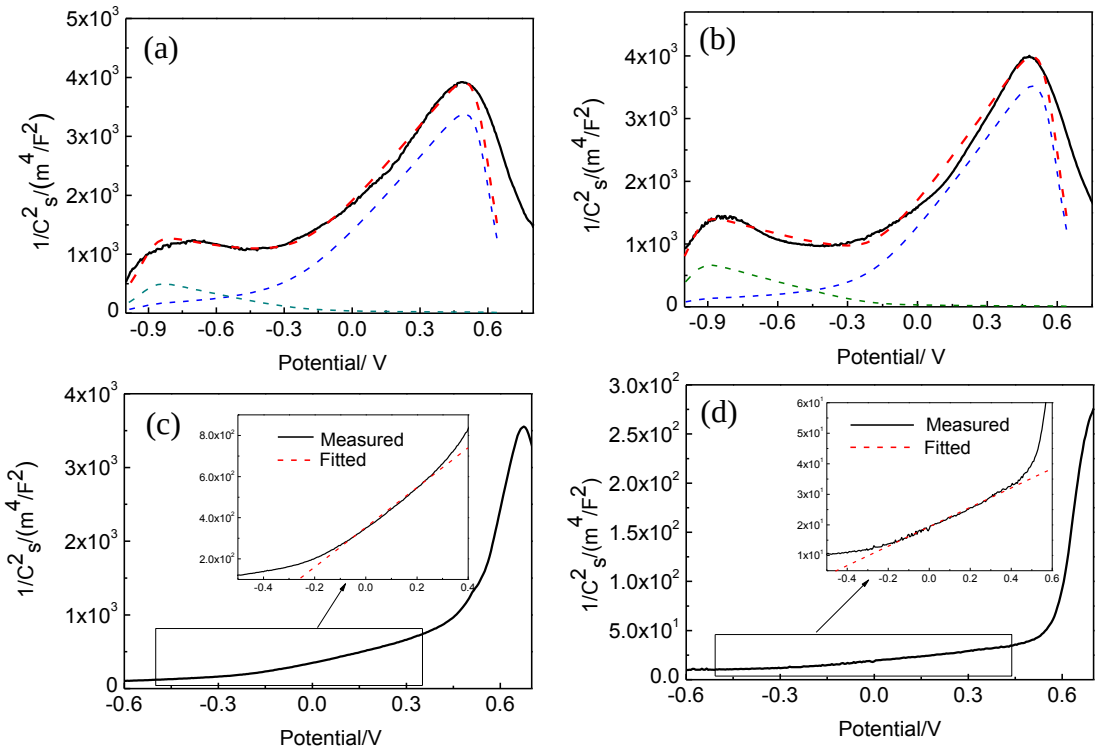

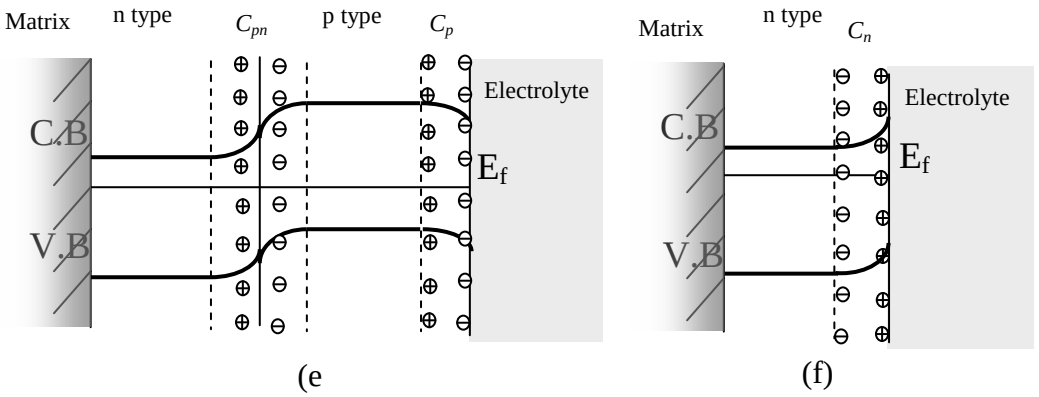

Figure 8. Mott–Schottky plots for the passive films formed on (a) the Incoloy 825 base metal and (b) the Inconel 625 weld bead in air and (c) the Incoloy 825 base metal and (d) the Inconel 625 weld bead after being corroded in an H_2S/CO_2 environment at 205℃. The schematic diagram of the band energy and space charge structures of the passive film with the bipolar double layers (e) and the unipolar n-type layer (f). Capacitance measurements were carried out by potentiodynamically sweeping from −1 to 0.8 V (vs. SCE) at 1 kHz. Polarization was applied in successive displacements of 50 mV.

After the HTHP H_2S/CO_2 corrosion at 205 ℃, only one positive linear slope is presented in the depletion region of the Mott–Schottky plots, as shown in Fig. 8(c) and Fig. 8(d). It can be concluded that the bipolar n-p type semiconductor characteristic of the passive film formed in air changes into a unipolar n-type. Based on the composition of the corrosion products formed in the HTHP H_2S/CO_2 environment at 205 ℃, as shown in Fig. 6(a), the semiconductor structure conversion of the passive film is most likely related to the transformation from an oxide film into a sulphide film. The band structure of the unipolar n-type film is illustrated in Fig. 8(f).

Based on the Mott–Schottky theory [38], the relation between the space charge capacitance (C_n) of an n-type semiconductor and the applied electrode potential (E) in the depletion region can be written as

$$C_n^{-2} = \frac{2}{eN_d \varepsilon \varepsilon_0 A^2}(E - E_{fb} - \frac{kT}{e}) \quad (1)$$

where ε is the dielectric constant of the passive film, ε_0 is the permittivity of free space (8.854×10^{-12} F/m), e is the electron charge (1.602×10^{-19} C), A is the sample area, N_d is the donor density, E_{fb} is the flat band potential, k is Boltzmann's constant (1.38×10^{-23} J/K), and T is the absolute temperature. kT/e can be neglected since it is only approximately 25 mV at room temperature.

According to Eq. 1, there is a linear relationship between C_n^{-2} and E in the depletion region. Then, the carrier density (N_d) in the film can be calculated based on the slope, and the corresponding results are shown in Table 5. For the Incoloy 825 base metal, the carrier density of the n-type film formed under the HTHP H_2S/CO_2 conditions is similar to that of the p-type outer layer of the air-formed bipolar film but larger than that of the inner n-type layer. However, the carrier density of the film formed on the Inconel 625 weld after corrosion under the HTHP H_2S/CO_2 conditions is two orders of magnitude larger than that of the film formed in air. Therefore, the HTHP H_2S/CO_2 conditions could degrade the compact density of the passive film, and the film on the Inconel 625 weld suffers a relatively more sever degradation.

Table 5. Carrier densities calculated from the Mott–Schottky plots of C^{-2} vs. E for the passive films.

	Without corrosion		After corrosion
	inner n-type semiconductor layer	outer p-type semiconductor layer	n-type semiconductor layer
Incoloy 825 base metal	2.4×10^{25} m^{-3}	9.7×10^{25} m^{-3}	9.8×10^{25} m^{-3}
Inconel 625 weld bead	2.2×10^{25} m^{-3}	8.1×10^{25} m^{-3}	2.7×10^{27} m^{-3}

4. DISCUSSION

The elemental contents of Ni, Cr, and Mo in the Inconel 625 alloy are much higher than those in the Incoloy 825 alloy. Therefore, the passive film grown on the Inconel 625 alloy in air possesses a higher compact density and shows a superior corrosion resistance. However, high content of alloy elements will lead to a high sensibility of precipitation [4-8]. As a result, the Laves and G phases will be precipitated in the interdendritic region of the Inconel 625 weld bead due to the segregation of Ni, Cr, Mo, and Nb elements during the solidification process. Both of these two phases contain less Cr content than the metal matrix. Cr is a key element enhancing the passivation ability of passive film on corrosion resistant alloys [39-41]. So, the depletion of Cr would reduce the corrosion resistance of passive film at the area where precipitates forms and then induce the localised corrosion or pitting. Furthermore, the SKPFM results demonstrate the obvious Volta potential difference where the Laves and G phase precipitates are located. So, the galvanic mechanism is established [29-34, 42-45], featuring the large ratio of the cathodic (matrix) to the anodic (precipitates) regions. Therefore, the Laves and G phases will suffer preferential corrosion.

Based on the point defect model (PDM) [35], Sato [36, 37] proposed a bipolar structure consisting of excess metal ions or oxygen ion vacancies in the inner layer, and excess oxygen ions or metal ion vacancies in the outer layer. From the electronic view, the hydroxides outer layer provides the negative fixed charge with a cation-selective property, which means that it can prevent anions in the solution to diffuse into the passive film, and shows p-type semiconductor. Correspondingly, the oxides inner layer provides the positive fixed charge with an anion-selective property, which can resist cations to migrate across the passive film to the solution, and presents n-type semiconductor [16, 46]. This sophisticated mechanism prevents the metal matrix from corrosive attack [36]. Before the air-formed passive films on the Inconel 625 and the Incoloy 825 are attacked by the corrosive media, they maintain a structure of bipolar semiconducting layers. Due to the air-formed passive film, the sensitive Laves and G phases could not be dissolved and the pitting corrosion is inhibited under moderate conditions. However, under the HTHP H_2S/CO_2 corrosive conditions at 205 ℃, the air-formed film structure can be broken and transforms from an n-p type bipolar semiconductor into an n-type unipolar semiconductor. This type of passive film can only prohibit the diffusion of cations at the interface and not anions, thereby causing an inferior protection compared with the bipolar film. Therefore, after the

passive film has been broken down, the Laves and G phases in the Inconel 625 weld bead will accelerate the localized corrosion rate and form pitting corrosion in combination with the galvanic mechanism.

5. CONCLUSIONS

(1) The Laves and G phases precipitate in the interdendritic region of the Inconel 625 alloy weld during the solidification process. Both the phases show depleted in Ni and Cr but are rich in Mo and Nb compared to the matrix metal.

(2) The SKPFM experiments demonstrate that the Laves and G phases have inferior corrosion resistance compared to the matrix metal and can establish the galvanic effect featuring a large ratio of cathodic to anodic areas on the matrix.

(3) Under the HTHP H_2S/CO_2 corrosive conditions at 205 ℃, the air-formed film could be broken and then transformed from an n-p type bipolar semiconductor film into an n-type unipolar semiconductor film. The Laves and G phases in the Inconel 625 weld bead accelerate the localized corrosion rate and cause pitting corrosion under the galvanic effect. The Inconel 625 weld presents more pits than the Incoloy 825 base metal, even though the Inconel 625 alloy has a higher content of corrosion-resistant elements.

ACKNOWLEDGEMENTS
This paper was supported by the National Key Basic Research Program of China (No. 51301200 and 51134011).

References

1. G. Book, M. Bates, *SPE Middle East Health, Safety, Security, and Environment Conference and Exhibition 2012*, Abu Dhabi, Paper No.154553.
2. D. Aberle, D. Agarwal, *NACE Corrosion 2008*, Houston, Paper No.08085.
3. P. Ganesan, C. Renteria, *J. Crum, Superalloys*, 718 (1991) 625.
4. G. Dinda, A. Dasgupta, J. Mazumder, *Materials Science and Engineering: A*, 509 (2009) 98.
5. C. C. Silva, H. C. de Miranda, M. F. Motta, J. P. Farias, C. R. M. Afonso, A. J. Ramirez, *Journal of Materials Research and Technology*, 2 (2013) 228.
6. M. Cieslak, T. Headley, R. Frank, *Welding Journal*, 68 (1989) 473.
7. F. Xu, Y. Lv, B. Xu, Y. Liu, F. Shu, P. He, *Materials & Design*, 45(2013) 446.
8. E. M. Zahrani, A. Alfantazi, *Corrosion Science*, 85 (2014) 60.
9. N. Ahmed, M. Bakare, D. McCartney, K. Voisey, *Surface and Coatings Technology*, 204 (2010) 2294.
10. A. Tuthill, R. Avery, *Welding Journal*, 72 (1993) 41.
11. K. Cooper, P. Slebodnick, E. Thomas, *Materials Science and Engineering: A*, 206 (1996) 138.
12. M. Bakare, K. Voisey, M. Roe, D. McCartney, *Applied Surface Science*, 257 (2010) 786.
13. C. Cuevas-Arteaga, D. Verhelst, A. Alfantazi, *ECS Transactions*, 28 (2010) 61.
14. H. Z. Rajani, S. A. Mousavi, F. M. Sani, *Materials & Design*, 43 (2013) 467.
15. D. W. I. C. Fink, I. M. Zinke, D. W.I. D. Keil, *Welding in the World*, 56 (2012) 37.

16. R. Jiang, C. Chen, S. Zheng, *Electrochimica Acta*, 55 (2010) 2498.
17. K. H. Lo, C. H. Shek, J. Lai, *Materials Science and Engineering: R: Reports*, 65 (2009) 39.
18. O. Chopra, G. Ayrault, *Nuclear engineering and design*, 86 (1985) 69.
19. N. Evans, P. Maziasz, R. Swindeman, G. Smith, *Scripta Materialia*, 51 (2004) 503.
20. M. Cieslak, G. Knorovsky, T. Headley, A. Romig Jr, *Superalloy*, 718 (1989) 59.
21. S. Li, Y. Wang, X. Wang, F. Xue, *Journal of Nuclear Materials*, 452 (2014) 382.
22. I. Shuro, H. Kuo, T. Sasaki, K. Hono, Y. Todaka, M. Umemoto, *Materials Science and Engineering: A*, 552 (2012) 194.
23. L. H. de Almeida, A. F. Ribeiro, I. L. May, *Materials Characterization*, 49 (2002) 219.
24. A. Mateo, L. Llanes, M. Anglada, A. Redjaimia, G. Metauer, *Journal of materials science*, 32 (1997) 4533.
25. B. Piekarski, *Materials characterization*, 47 (2001) 181.
26. M. Stratmann, H. Streckel, *Corrosion Science*, 30 (1990) 681.
27. M. Stratmann, H. Streckel, *Corrosion Science*, 30 (1990) 697.
28. M. Stratmann, H. Streckel, K. Kim, S. Crockett, *Corrosion Science*, 30 (1990) 715.
29. P. Schmutz, G. S. Frankel, *Journal of The Electrochemical Society*, 145 (1998) 2285.
30. P. Schmutz, G. S. Frankel, *Journal of The Electrochemical Society*, 145 (1998) 2295.
31. V. Guillaumin, P. Schmutz, G. S. Frankel, *Journal of The Electrochemical Society*, 148 (2001) B163.
32. P. Leblanc, G. S. Frankel, *Journal of The Electrochemical Society*, 149 (2002) B239.
33. N. Sathirachinda, R. Pettersson, S. Wessman, U. Kivisäkk, J. Pan, *Electrochimica Acta*, 56 (2011) 1792.
34. E. Bettini, T. Eriksson, M. Boström, C. Leygraf, J. Pan, *Electrochimica Acta*, 56 (2011) 9413.
35. D.D. Macdonald, M. Urquidi-Macdonald, *Journal of The Electrochemical Society*, 137 (1990) 2395.
36. N. Sato, *Corrosion*, 45 (1989) 354.
37. N. Sato, *Corrosion science*, 31 (1990) 1.
38. S.R. Morrison, *Electrochemistry at Semiconductor and Oxidized Electrodes*, Plenum Press, New York (1980).
39. C. Boissy, B. Ter-Ovanessian, N. Mary, B. Normand, *Electrochimica Acta*, 141 (2015) 430.
40. Antoine Seyeux, Sandrine Zanna, Audrey Allion, Philippe Marcus, *Corrosion science*, 91 (2015) 352.
41. Tianshu Li, Li Liu, Bin Zhang, Ying Li, Fuhui Wang, *Corrosion science*, 111 (2016) 186.
42. Jiong Qian, Changfeng Chen, Haobo Yu, Feng Liu, Hong Yang, Zhonghua Zhang, *Corrosion science*, 111 (2016) 352.
43. Jinhui Liu, Yingwei Song, Jiachen Chen, Peng Chen, Dayong Shan, En-Hou Han, *Electrochimica Acta*, 189 (2016) 190.
44. Q.N. Song, Y.G. Zheng, D.R. Ni, Z.Y. Ma, *Corrosion science*, 92 (2015) 95.
45. Ali Davoodi, Zohreh Esfahani, Madjid Sarvghad, *Corrosion science*, 107 (2016) 133.
46. Ruijing Jiang, Yuwu Wang, Xu Wen, Changfeng Chen, Jingmao Zhao, *Applied Surface Science*, 412 (2017) 214.